Residual Stresses in a Quenched Superalloy Turbine Disc: Measurements and Modeling

M.A. RIST, S. TIN, B.A. RODER, J.A. JAMES, and M.R. DAYMOND

A series of neutron diffraction measurements have been carried out to determine the elastic residual strains deep within a large, 40-cm-diameter, forged and water-quenched IN718 aeroengine compressor disc. Neutron path lengths of up to 6 cm were necessary to probe the thickest parts of the forging, and three-dimensional strain and stress components have been derived for the first time in such a large superalloy specimen. Measurements have been compared with the results from a coupled thermal-mechanical finite-element model of the quenching process, based upon appropriate temperature-dependent material properties, with some success. The general residual stress state in the disc is one of near-surface compression, balanced by tension within the disc interior. The steepest stress and strain gradients occur in the transition region from compression to tension, about 1 cm below the surface all around the disc. The largest stress component is in the disc tangential direction and reaches a magnitude of 400 to 500 MPa near the disc surface and at its core. This exceeds the effective yield stress because of the presence of significant hydrostatic stress.

I. INTRODUCTION

THE production of modern gas turbine discs for aerospace applications involves multiple manufacturing steps carried out to rigorous specification. A typical processing route involves casting and refinement of the ingot *via* hot deformation with open and closed dies, followed by heat treatment and then a series of machining operations. The robust design of critical rotating aeroengine components requires these materials to possess exceptional structural integrity, and tight control is maintained over the material microstructure, defect content, and mechanical properties. To assist with quality control and cost savings, computational simulations of the various processing steps are often utilized to optimize the processing parameters (*e.g.*, References 1 through 4), and significant progress has now been made with the development of integrated models covering several manufacturing stages.[5,6] Validation of such models has concentrated mainly on microstructural changes occurring during each stage of the manufacturing process. On the other hand, proper assessment of deep residual stresses created during postforging heat treatment of superalloys has proven rather more elusive. The difficulty arises because conventional diffraction methods, used for deducing internal stresses from crystallographic lattice strains, have hitherto proved somewhat ineffective—even neutrons have relatively weak penetration in nickel superalloys when compared to steels, for example. The near-surface stress state can be deduced using laboratory X-rays or hole-drilling methods, for instance, but deeper material removal methods and through-thickness ultrasonic probing techniques are prone to high degrees of inaccuracy. Now, using ENGIN-X, the new engineering diffractometer at the ISIS pulsed neutron source in the United Kingdom,[7] internal stresses can be precisely measured to greater depths than was previously possible. This has enabled through-thickness probing of a full-scale, nickel superalloy compressor disc to be carried out. Accurate quantification of the residual stress field in the heat-treated and quenched disc crucially allows elastic relaxation to be accounted for during subsequent machining operations, which can then be carried out to maintain optimum dimensional tolerances.

Although a significant number of experimental and numerical studies have been undertaken to examine heat-treatment residual stresses in steel components (*e.g.*, References 8 through 10), relatively few published works have looked at nickel-based superalloys. Wallis and Bhowal[11] have reported results from finite-element analyses used to model the temperature and stress evolution in superalloy turbine disc forgings subjected to forced air and oil quenching. Although their model output showed good correlation between the predicted and measured temperature evolution, the predicted stresses were not directly validated. Franchet *et al.*[12] also used the finite-element method to optimize quenching of Astroloy powder discs. They deduced that the use of an elastic-plastic material model is adequate for describing superalloy constitutive behavior, since the strain due to transformation plasticity is negligible. Model results showed reasonable agreement with surface radial and tangential stresses deduced from surface strain-gage measurements. Dye *et al.*[13] have carried out similar analyses on small, 2-cm-diameter, cylindrical bars of IN718 quenched in oil, water, and air, validated against neutron diffraction measurements of the three-dimensional stress field made at the cylinder midsection. Neutron strain scanning has also recently been used by Cihak *et al.*[14] to assess the residual stress state in a full-sized forged and water-quenched IN718 turbine disc. Three perpendicular lattice-parameter measurements were made at several locations within the ~25-mm-thick disc, but the stress-free lattice parameter was not obtained. The magnitudes of the radial and tangential stresses were inferred by assuming that the axial stress component was zero over most of the disc radius.

M.A. RIST, Lecturer, and J.A. JAMES, Researcher, are with the Department of Materials Engineering, The Open University, Milton Keynes, MK7 6AA, United Kingdom. S. TIN, Assistant Director of Research, and B.A. RODER, Student, are with the Rolls-Royce University Technology Partnership, Department of Materials Science and Metallurgy, University of Cambridge, Cambridge CB2 3QZ, United Kingdom. M.R. DAYMOND, Research Chair, is with the Department of Mechanical and Materials Engineering, Queen's University, Kingston, ON, Canada, K7L 3N6.

Manuscript submitted April 25, 2005.

In the current article, we present the results from a series of neutron diffraction measurements within a 40-cm-diameter, commercially produced IN718 nickel-superalloy aero-engine turbine disc forging. Diffraction-path lengths of up to 6 cm were used at ENGIN-X to probe even the thickest (~4.5 cm) parts of the forged and quenched disc, and full three-dimensional stress and strain components have been derived for the first time in such a large superalloy specimen. The magnitude and character of the three-dimensional residual stress state induced by nonuniform thermal contraction is examined, and results have been used to validate a coupled thermal-mechanical finite-element model of the quenching process.

II. EXPERIMENTAL DETAILS

A. *Material*

The disc material studied was IN718, a nickel-based superalloy widely used in turbine components because of its excellent high-temperature mechanical properties. The major alloying constituents of the material are 19 pct Cr, 18 pct Fe, 5 pct Nb, 3 pct Mo, 1 pct Ti, and 0.5 pct Al (nominal wt pct). The alloy derives its in-service strength mainly from precipitation (below 900 °C) of coherent intermetallic phases: the niobium-rich bct γ'' phase and, to a lesser extent, the aluminium-rich fcc γ' phase. Precipitation of the orthorhombic δ phase is also important at hot-working temperatures above 900 °C, where its presence can be used to control grain size through grain-boundary pinning.

Following a commercial processing route,[5,6] the forged disc was subjected to a standard solution heat treatment, during which the δ precipitates were partially returned into solution. The disc was then rapidly cooled by quenching in water. Subsequently, a small amount of material was machined from the bore of the disc by the manufacturers, at which point the component was made available for examination using neutron diffraction as described in this article. It was assumed that the removal of material at the bore of the disc would have negligible effect at large disc radii; however, the consequences of this assumption will be discussed in Section IV.

Microstructures of the as-quenched forging were analyzed and found to consist of fine, equiaxed single-phase γ-nickel grains, and a small fraction of δ precipitates distributed along the grain boundaries (Figure 1). Both scanning electron microscopy and transmission electron microscopy (SEM and TEM, respectively) revealed no precipitates of γ' and γ'' present within the grains of the as-quenched forging (these strengthening phases are later introduced during stress-relief and aging heat treatments, prior to final joining of the turbine component). The microstructure was uniform throughout the forging, with a normal grain-size distribution and an average grain size of approximately ASTM 11 (7 μm).

B. *Neutron Diffraction Measurements*

Mapping the strain at different positions within a component of complex geometry requires careful planning, particularly to minimize the path length of the neutron beam within the specimen and, hence, to reduce measurement times. Precise definition of the specimen geometry is also necessary, along with correct transformation of positional measurements between the specimen and instrument coordinate systems. To this end, a two-dimensional cross-sectional profile of the disc surface, accurate to within 10 μm, was obtained using a digital coordinate measurement machine fitted with a spherical contact probe, and the three-dimensional geometry of the disc was defined by assuming axisymmetry. In the current article, a cylindrical coordinate system has been used in which the local radial (r) and tangential, or "hoop", (θ) directions vary with angular position around the disc axis (z), as illustrated in Figure 2.

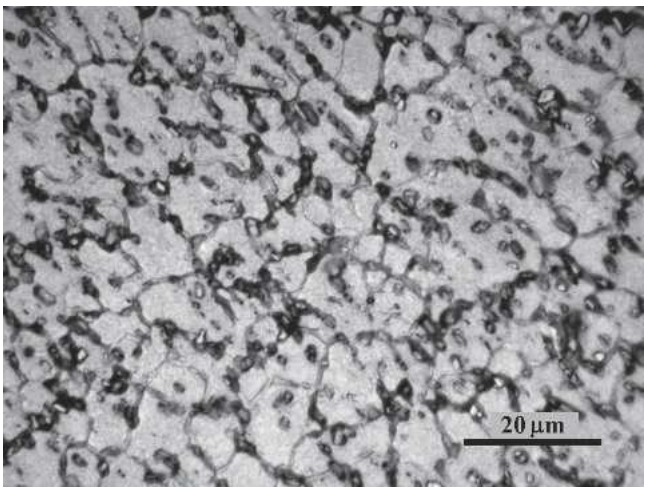

Fig. 1—Microstructure of the as-quenched IN718 forging, showing grain-boundary δ and equiaxed grains of the γ phase.

Strain measurements were carried out using the ENGIN-X diffractometer at ISIS, specifically designed to accommodate measurements on engineering components and structures.[7] The instrument uses the "time-of-flight" technique, in which neutrons with a continuous range of wavelengths and, hence, velocities are directed at the specimen. Flight times of diffracted neutrons are recorded at a fixed-position detector, and a diffraction spectrum, of intensity *vs* flight time or wavelength, is generated. Because of the polychromatic nature of the incident beam, all lattice planes in a polycrystalline specimen contribute to the measured spectrum, according to Bragg's law. Peaks in intensity correspond to reflections from a certain family of grains, oriented such that a particular set of crystal lattice planes diffracts to the detector. Measurement of the positions and intensities of the diffraction peaks allows lattice spacings to be calculated, provided the crystal structure is known. In this study, the Rietveld method was used to fit a number of peaks over a range of suitable lattice spacings chosen in order to a obtain strain representative of the bulk polycrystalline material. Four peaks were used, corresponding to scattering from the (111), (200), (220), and (311) crystallographic planes. The use of these peaks during Rietveld refinement has been shown empirically to be a good procedure for averaging out intergranular strains in fcc materials undergoing {111}<110> octahedral slip, at least for elastic-plastic strains up to about 2 pct.[15,16] The average lattice spacing (d) was then used to calculate the strain component in the direction of the diffraction vector as $\varepsilon = (d - d_0)/d_0$, where d_0 is the stress-free lattice parameter. In fact, the ENGIN-X apparatus uses two fixed sets of detectors, each at 90 deg to the incident beam, allowing strain to be recorded in two

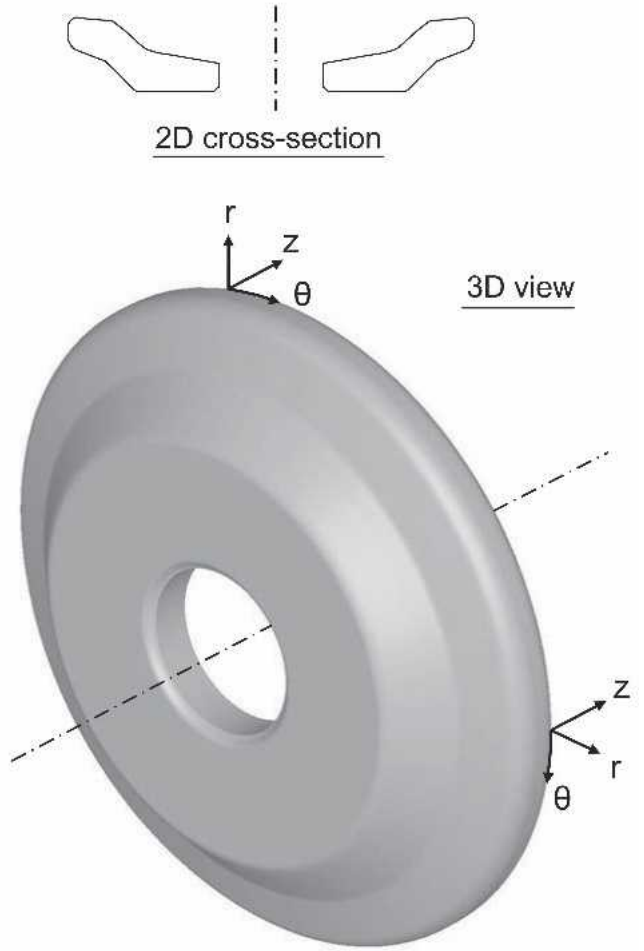

Fig. 2—Disc geometry showing the axial (z), radial (r), and tangential/hoop (θ) directions. The outside diameter of the disc is 400 mm.

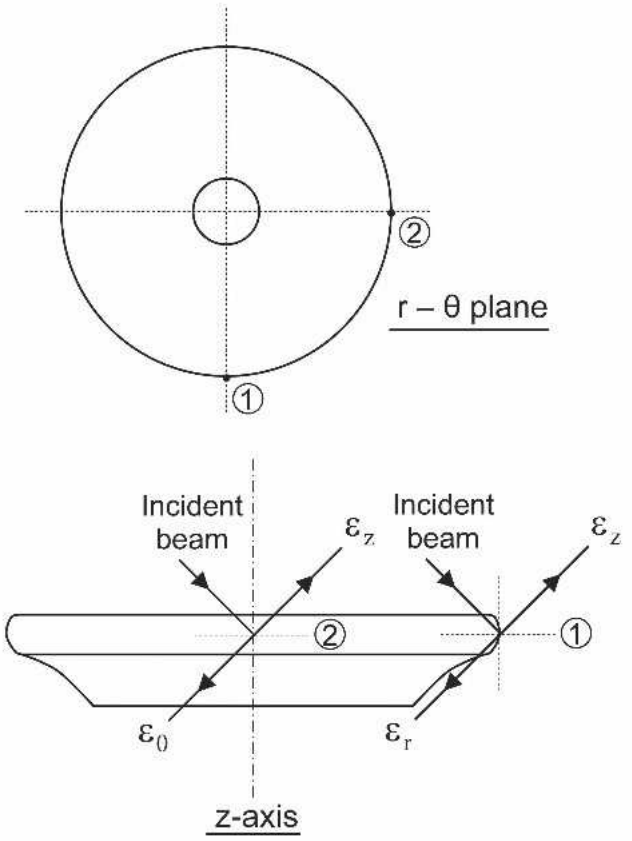

Fig. 3—Sketch showing the scheme for obtaining strain components from neutron scattering in the disc, with its face vertical and at 45 deg to the horizontal incident beam. The state of strain at locations 1 and 2 should be identical, assuming axisymmetry.

directions simultaneously. Measurements were made by placing the cylindrical face of the disc vertically and at 45 deg to the horizontal incident beam, as illustrated in Figure 3. This allowed two perpendicular components of strain to be deduced at each measurement position: the axial strain (ε_z) and either the hoop or radial strain (ε_θ or ε_r, respectively). By repeating measurements at the same (r,z) coordinates separated by an angle of 90 deg, *e.g.*, positions 1 and 2 near the rim of the disc in Figure 3, it was possible to obtain the three mutually perpendicular strain components plus a second measurement of the axial component. The repeatability of the latter measurements was a useful confirmation that the assumption of axisymmetry was valid.

The full program of measurement locations is shown in Figure 4. Scans were planned and mapped in the specimen coordinate system and automatically converted to the instrument coordinate system using dedicated software.[17] Measurements of the axial, hoop, and radial strains were made along the scan lines AB and EF; axial and hoop strains were measured along the lines CD, GH, and IJ. The strain measured at each nominal point, accurate to within 0.1 mm, was the average taken within a sampled gage volume centered on that point, as defined by the intersection of the incident and diffracted neutron beams. This could be adjusted using a neutron-absorbing aperture in the incident beam path and by radial collimation of the diffracted beam. In order to obtain representative strain measurements in a reasonable time and to avoid variations due to sampling of a small number of grains, the measurements were made from gage volumes between 4 × 4 × 4 and 4 × 4 × 10 mm, dependent upon the position within the specimen. All measurements were made using gage volumes that were completely filled by the sample material.

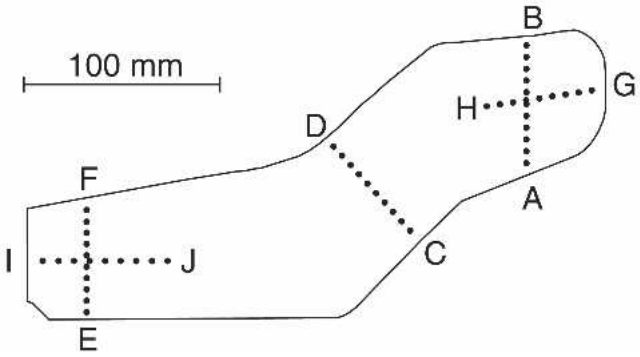

Fig. 4—Positions of strain measurements made in the disc, shown on the plane of symmetry.

A key consideration in making neutron diffraction strain measurements is the correct characterization of the stress-free lattice parameter (d_0). For this purpose, two small prismatic specimens, with end dimensions of 3 × 3 mm, were cut through the thickness of the disc close to the bore and rim using an electrodischarge machine. These specimens were then cut transversely into small, partially attached segments,

forming a stress-relieved comb structure. Diffraction measurements on the combs were made using each of the two instrument detector arrays in order to estimate d_0 in orthogonal directions. This produced values from the [left/right] detector pair of d_0 = [3.603064/3.602628] Å at the inner bore and d_0 = [3.602573/3.602767] Å at the outer rim. There was no significant variation of measurement between orthogonal directions, indicating material isotropy, or between the specimens cut from the bore and rim, implying homogeneity across the disc radius. Hence, a mean value and standard deviation for the reference lattice parameter of $d_0 = 3.60380 \pm 0.00022$ Å was used to compute strain.

III. FINITE-ELEMENT ANALYSIS

A two-dimensional axisymmetric finite-element model of the quenching process was implemented using DEFORM software,[18] a simulation system designed specifically for the examination of forming and heat-treatment processes. The model was based upon a 3000-element mesh of the disc geometry (Figure 5) and incorporated a fully coupled thermal-mechanical analysis of elastic-plastic deformation and heat transfer. Within DEFORM, a skyline matrix-storage scheme was used in conjunction with Gaussian elimination for efficient solution of the finite-element matrix equations, and the Newton–Raphson iteration method was used to determine the nodal velocity and force convergence.

A rate-independent elastic-plastic constitutive model was used to describe the material deformation behavior. Plastic flow under complex loading was characterized using a temperature-dependent initial yield stress (σ_y) coupled with an isotropic linear hardening coefficient (H), such that the effective (von Mises) flow stress was given by $\bar{\sigma} = \sigma_y + H\bar{\varepsilon}$, where $\bar{\varepsilon}$ is the effective strain. The room-temperature uniaxial yield stress of the solution-treated IN718 is approximately 360 MPa,[19] and this value was assumed to show the same proportional decrease with temperature as that measured for fully heat-treated IN718,[20] falling to around 10 pct of its room-temperature value at 1000 °C, with the steepest decrease occurring above about 700 °C (Figure 6). This yield behavior is similar to that recently used elsewhere to model residual-stress evolution in IN718.[13,21] A value of H = 100 MPa was assigned to simulate appropriate strain hardening, although it was found that the model results were quite insensitive to this parameter: varying H by an order of magnitude altered the predicted stress state by less than 5 pct. Since the magnitude of the elastic modulus of IN718 varies little with thermal history, temperature-dependent values for the commercially produced alloy[22] were used. Similarly, values for the other temperature-dependent thermal properties (expansivity, heat capacity, and thermal conductivity), all of which depend on crystallography rather than microstructure or heat treatment, were taken from tables of recommended values for the commercial alloy;[23] the Poisson's ratio was assumed to be constant at 0.3.

The convection coefficient for heat transfer between the disc material and quenchant was estimated from cooling curves recorded during water quenching of a thermocoupled 60-mm-diameter bar of IN718. A finite-element model of the bar geometry was created, using the material properties detailed previously, and the convection coefficient was adjusted to give good agreement between the measured and predicted surface cooling rate at the bar midpoint. Quenching in water can lead to apparently erratic cooling behavior, reflecting complex changes in the heat-transfer coefficient associated with vapor bubble formation, boiling, and convection. However, a satisfactory empirical fit to the observed cooling was achieved, as illustrated in Figure 7, using a constant value for the convection

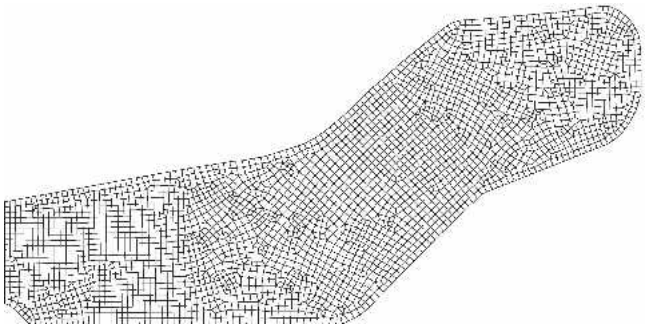

Fig. 5—Finite-element mesh of the axisymmetric disc geometry, consisting of 3000 four-node quadrilateral elements.

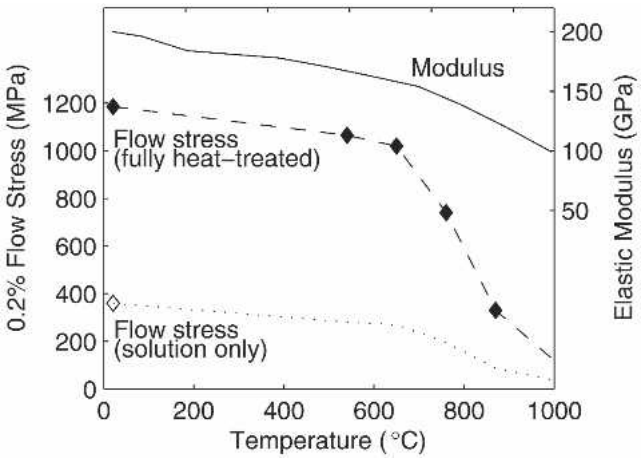

Fig. 6—Flow-stress[19,20] and elastic-modulus[22] data used in the finite-element model of the quenching process.

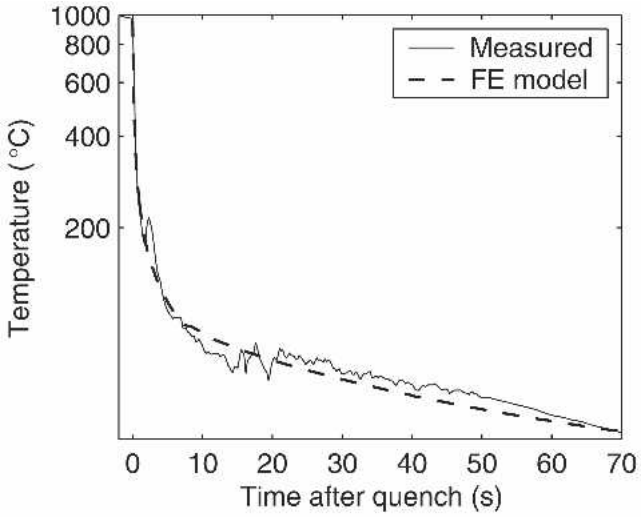

Fig. 7—Measured and predicted surface cooling curves for a water-quenched IN718 solid cylindrical bar.

coefficient of 20 kW m^{-2} K^{-1} above 100 °C, falling linearly below this temperature to 2 kW m^{-2} K^{-1} at 25 °C. During modeling of the full disc-quenching process, the brief (~30 seconds) transfer period from furnace to quenchant was also simulated. For this purpose, a still-air convection coefficient of 0.01 kW m^{-2} K^{-1} was used in conjunction with a radiative emissivity of 0.7, appropriate for nickel alloys with an oxide coating.[24]

IV. RESULTS AND DISCUSSION

The strain components derived from neutron diffraction measurements along each of the disc scan lines are plotted as solid symbols in Figure 8. The measurement error bars are derived from the standard deviation associated with least-squares fitting of theoretical intensities to measured neutron diffraction peaks, *i.e.*, they reflect the accuracy with which the lattice spacing could be determined at each measurement point. Large error bars are generally associated with less accessible parts of the disc and long effective diffraction-path lengths, although this was partly compensated for by using longer data-acquisition times as appropriate. The trend lines in Figure 8 represent the finite-element model predictions of the corresponding residual elastic-strain components, after the quenched disc had cooled to room temperature.

Overall qualitative agreement between the measured and predicted variations of the three strain components is good. Along all scan lines, both hoop and radial strains are compressive near the disc surface and become increasingly tensile with depth. Axial strains mirror this trend along the lines AB and EF, parallel to the disc axis, but are more erratic elsewhere. Generally, the measured maximum and minimum strains correspond well with those predicted by the finite-element model, and only minor offsets (2 to 3 mm) appear between the observed and predicted locations of the steeper strain gradients. However, along line IJ (Figure 8(e)) it can be seen that the predicted transition from compressive to tensile hoop strain (solid line) is offset from the measurements (triangular symbols), toward the inner rim, by a greater amount (about 6 to 7 mm). In other words, the region of compressive hoop strain extends to greater depths along this line than what is predicted by the model. This is also reflected in the disagreement between the magnitude of the predicted and measured hoop strain along line EF (Figure 8(c)). The discrepancy is probably due to the postquench machining of the inner bore, which is not accounted for in the current model. It is also possible that there may be variations in the heat-transfer properties of the disc surface, or in the temperature of the quenchant in the confined space at the disc bore. Nevertheless, the error in locating the tensile-compression transition of the hoop-strain component in this region is relatively small on the scale of the disc and does not detract from the following discussion.

An estimate of the residual stress state can be made along the scan lines for which three orthogonal strain measurements were carried out. Axisymmetry dictates that only the hoop component is a principal strain, and a knowledge of a fourth nonzero component (the shear strain in the plane of r and z (ε_{rz})) is strictly necessary to complete the full strain tensor, from which the stress state can then be computed. However, it is not unreasonable to assume that the shear component is small along the lines AB and EF, where the normal to the upper and lower surfaces is roughly parallel to the disc axis, *i.e.*, ε_r and ε_z, can also be considered as principal strains. The corresponding principal stresses can then be calculated using room-temperature values for the Young's modulus (E) and Poisson's ratio (ν), using a generalized version of Hooke's law:

$$\sigma_r = \frac{E}{(1+\nu)(1-2\nu)}\left[(1-\nu)\varepsilon_r + \nu(\varepsilon_z + \varepsilon_\theta)\right]$$

with cyclic permutations for σ_z and σ_θ. Results are presented in Figure 9; note that here, the measurement error bars reflect the contribution of all three measured strain components to each component of stress. Finite-element model predictions, which do not make the zero-shear-stress assumption, are also shown in this figure, and it can be seen that the shear stress for σ_{rz} along these lines is not entirely insignificant, reaching ~150 MPa in places. Nevertheless, overall agreement is reasonable, particularly along line AB, where the trend and magnitudes of the significant hoop and radial stresses are well predicted. On the other hand, there is a notable difference between the maximum values of the measured and predicted hoop stresses along line EF, corresponding to the discrepancy in the depth of compressive hoop strain in this region, as discussed previously. However, even here the surface stresses are in reasonable agreement. This can be further demonstrated by considering the effective stress. This is predicted by the finite-element model to be 360 MPa at the extremities of both AB and EF; this value corresponds to the room-temperature yield stress of IN718 used in the model (Figure 6) and is the expected maximum effective stress that can be sustained in the component deformed to small strains. The experimental measurements estimate the effective stress to be 380 to 410 MPa at the same positions—a reasonable agreement, considering the simplicity of the isotropic linear hardening law used, which does not take account of possible high-temperature rate sensitivity, and given that the actual yield behavior might also differ from that assumed in Figure 6. It can, therefore, be concluded that the finite-element model provides a satisfactory representation of the stress distribution in the quenched disc.

Note that that large residual stresses can cause significant distortion during subsequent machining operations, but do not significantly influence the structural integrity of the final component, which undergoes further stress-relief and aging heat treatments prior to being placed in service. However, correct quantification of these stresses is crucial in validating the thermal-mechanical model presented here and will allow future processing routes to be successfully optimized.

To further summarize the pattern of residual stress within the component, it is instructive to examine a profile through the disc midthickness (line $L_1L_2L_3L_4$ in Figure 10(a)). The predicted postquench internal stress components, along with the von Mises effective stress, are presented in Figure 10(b). The effective stress is a measure of the magnitude of average deviatoric stress and is always taken to be positive, but the other signed stress components indicate that the entire internal core of the disc is in tension, while the periphery is in compression (refer also to Figure 9). Such a balance is necessary to maintain static equilibrium. Note that the effective stress is equal to the room-temperature yield stress of the alloy (360 MPa) almost throughout the entire disc,

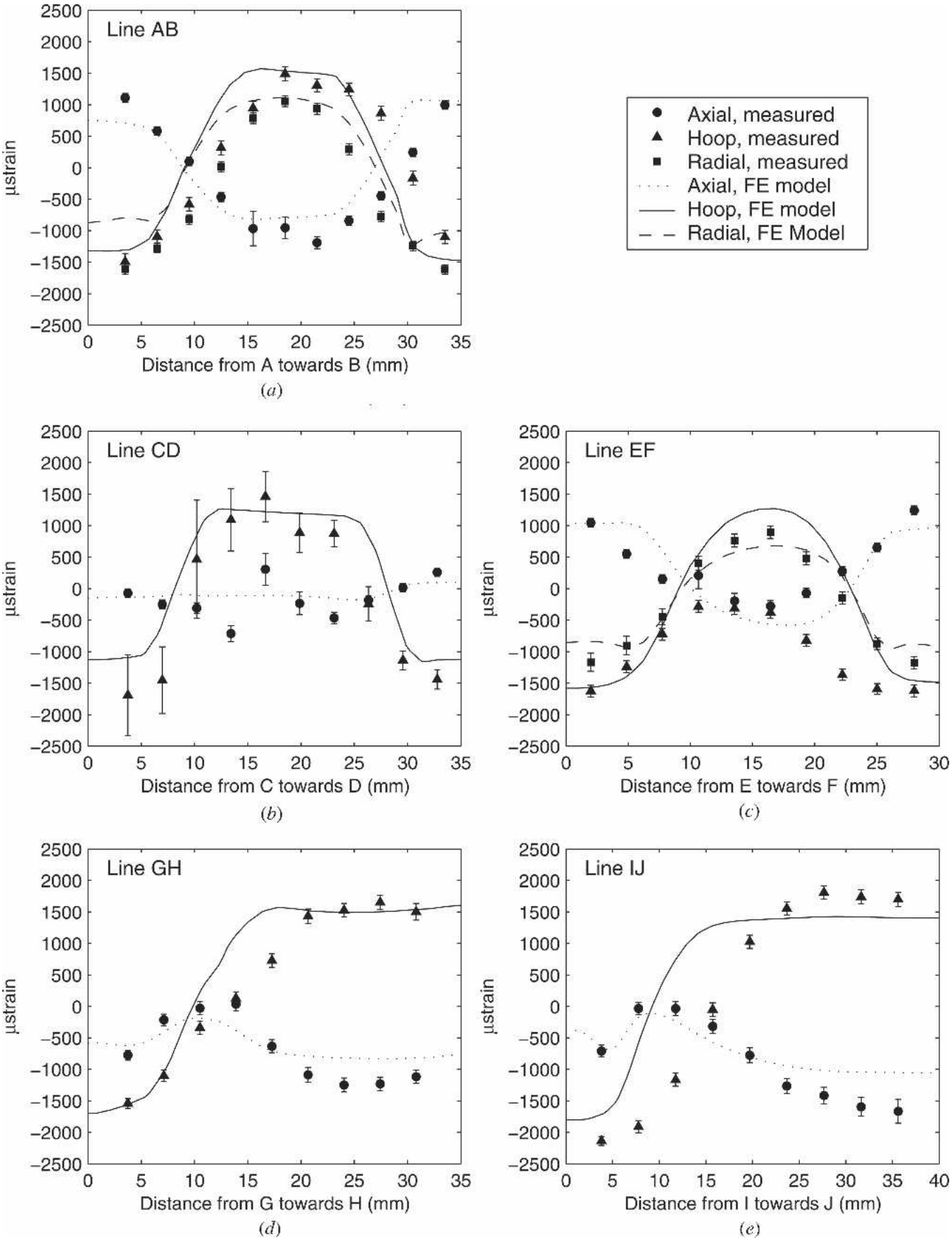

Fig. 8—Measured and predicted residual elastic strain components along disc scan lines.

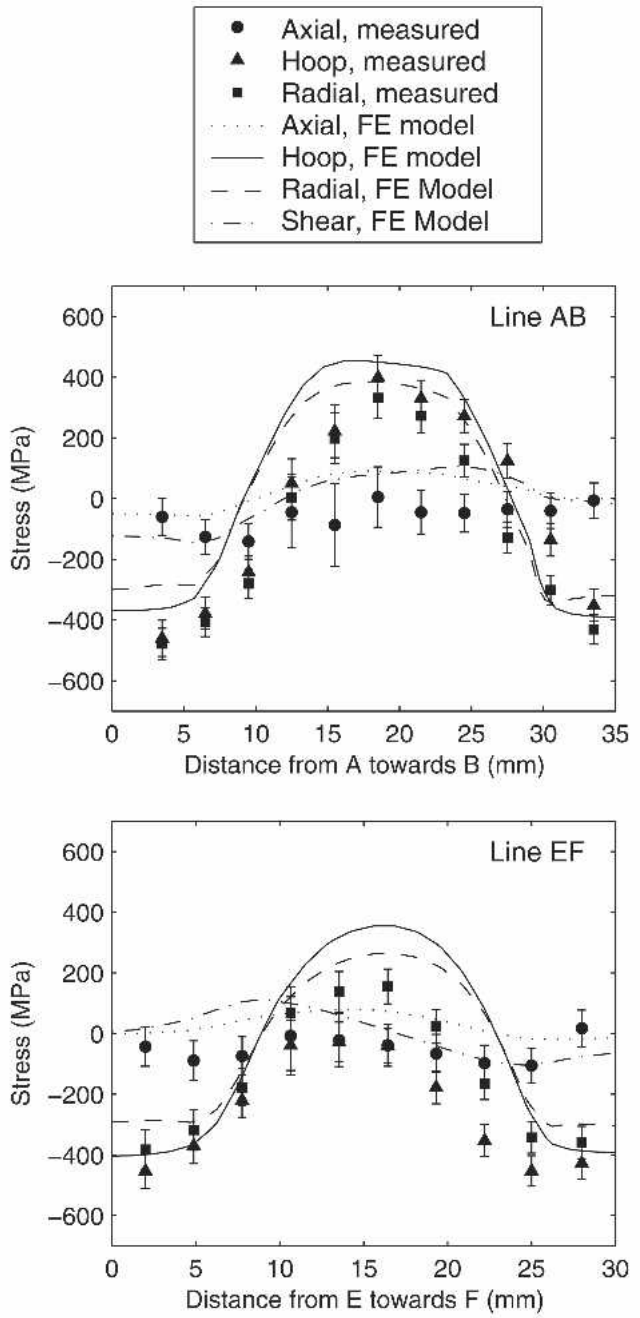

Fig. 9—Residual stress components derived from strain measurements and from finite-element model predictions.

except at a distance of about 10 mm below the disc surface, corresponding to the location of the tension-compression transition. Hence, it is clear that the magnitude of the final residual stress state is crucially dependent upon the room-temperature yield stress.

Of the individual components, the radial and hoop stresses are the major stresses throughout most of the disc, the latter reaching more than −400 MPa (compression) at the disc surface and approaching 500 MPa (tension) within the core. These values are greater than the magnitude of the effective yield stress because they are total (nondeviatoric) stresses and include a significant contribution from the local hydrostatic stress.

Figure 10(b) also shows that the radial stress is close to zero at the inner bore and at the outer rim; this is the expected

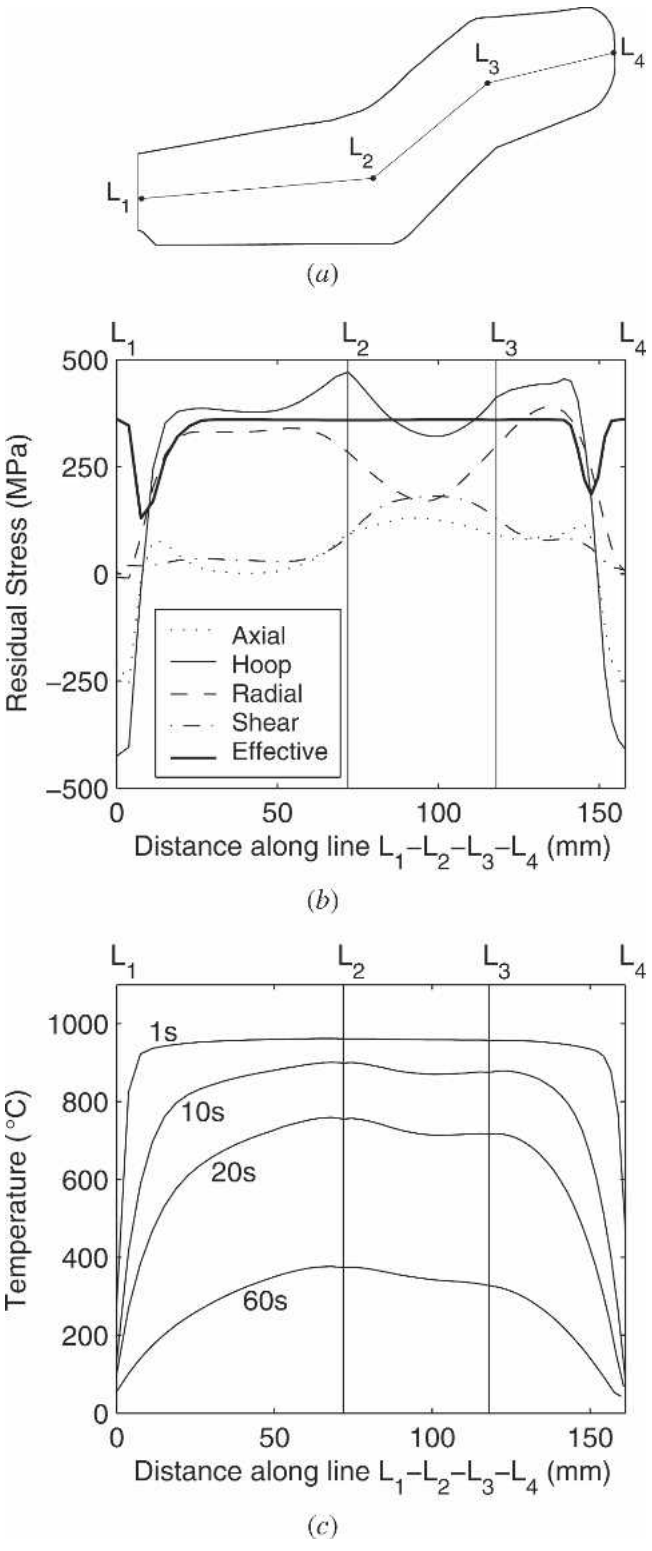

Fig. 10—Model predictions of the stress and temperature distribution along line $L_1L_2L_3L_4$ through the disc midthickness: (*a*) line location, (*b*) residual stress distribution, and (*c*) temperature distribution at various times following immersion in water quenchant.

free-surface boundary condition here. As a result of this constraint, there is significant compressive axial stress in these regions, almost −250 MPa. The predicted shear-stress component is also close to zero at the profile extremities and is

relatively small elsewhere, except in the inclined region between L_2 and L_3, where it reaches 180 MPa, indicating a susceptibility of the disc to bending. Note that the inclined upper and lower surfaces, parallel to the L_2L_3 segment, impose a partial constraint on the radial stress in this region, thus, inducing the large shear stress.

The temperature profile along $L_1L_2L_3L_4$ is shown in Figure 10(c), and it can be seen that there is a remarkably uniform internal-temperature distribution for the first few seconds after water quenching, despite significant cooling of the near-surface material. During this period, heat loss from the disc center is limited by the intrinsic thermal properties of the material rather than the (very high) convective heat-transfer coefficient. Nevertheless, even in the center of the disc, the total time for cooling to below 500 °C is well under 60 seconds. Such cooling rates are sufficiently high to suppress precipitation of γ'' phase,[25] consistent with microstructural observations (Section II–A).

The residual stress state can be rationalized by comparing the predicted evolution of the thermal and mechanical state within the disc interior and at the disc outer edge. Internal stresses arise due to differences in elastic and plastic mechanical properties created by the existence of thermal gradients. Figure 11 presents temporal changes in temperature, stress, and plastic strain at points L_3 and L_4 along $L_1L_2L_3L_4$. The unconstrained hoop component is used for illustrative purposes in this figure, because it is the dominant stress component throughout the disc (Figure 10(b)); the mean stress shows an identical trend. During the first 30 seconds, the disc undergoes air cooling as it is transferred from the furnace, and the temperature difference between L_3 and L_4 is relatively small. Nevertheless, the outside of the disc undergoes greater thermal contraction and places the disc interior in increasing compression; to maintain equilibrium the outer part of the disc experiences a balancing tensile stress. Figure 11 indicates that the plastic hoop strain remains at zero up to this point, so deformation is purely elastic. After 30 seconds the disc is immersed in water, and the outer part of the disc initially cools rapidly, while the temperature at the center changes little. The near-surface tensile stress increases sharply, and yield occurs first at L4, followed immediately by plastic flow within the disc interior at L3; the local stress is then limited by the temperature-dependent flow stress of the alloy. The rate of cooling at the disc core only starts to increase when the near-surface cooling begins to slow significantly. This means that contraction of the disc interior is resisted by the essentially noncontracting exterior, and, hence, the center starts to experience an increasingly tensile stress. Equilibrium dictates that the stress in the outer regions should simultaneously become more compressive, and Figure 11 shows that the sign of the stresses at L3 and L4 reverses, so that the final residual state of outer compression and inner tension is reached. Such stress-reversal behavior is generally consistent with the well-known transient behavior in quenched cylindrical bodies.[26] Although the magnitude of the residual stresses is governed by the room-temperature yield strength of the material, the precise location of the transition from compression to tension with depth is dictated by the thermal history of the forging.

Overall, the qualitative and quantitative agreement between the residual stress state inferred from the strain measurements and that predicted by the model of the quenching process can be regarded as satisfactory. Ongoing investigations are aimed at providing better data concerning the crucial temperature-dependent flow behavior specific to the as-quenched microstructure in the forging. Coupling of this data with measurements of the thermal boundary conditions during quenching of the disc itself would help to optimize the finite-element model and further improve its predictive capability.

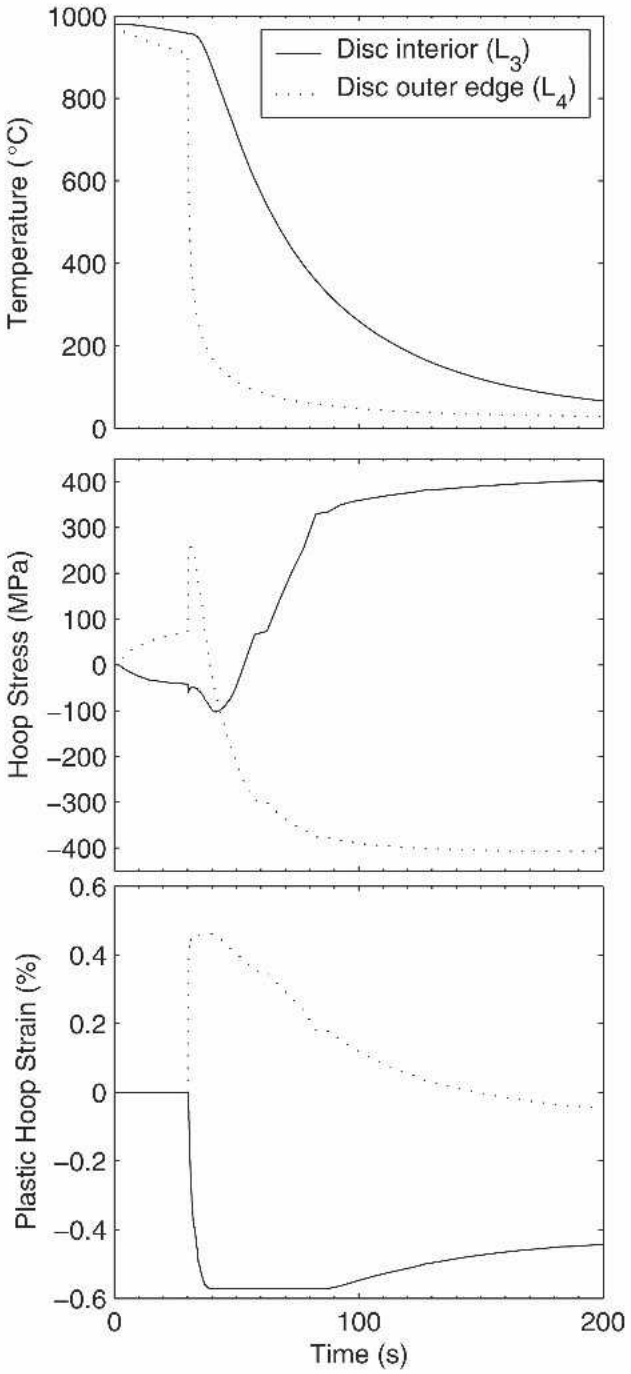

Fig. 11—Evolution of the temperature, hoop stress, and plastic hoop strain at L_3 and L_4 (Fig. 10(a)) during the first 200 s of the quenching process, including initial air cooling. Immersion in water occurs after 30 s.

V. SUMMARY AND CONCLUSIONS

Results from neutron strain-scanning measurements have been compared to those from a numerical model for predicting

residual stress after postsolution water quenching of a forged IN718 nickel superalloy aeroengine disc. The following conclusions can be drawn from the work.

1. The magnitude and variation of residual strains measured using neutron diffraction were found to be in good general agreement with those predicted by finite-element analysis, thus validating the model as a predictive tool. Machining at the disc inner bore had apparently shifted the local hoop-strain field to some degree, but the positions of major gradients in the residual strain agreed to within a few millimeters throughout the forging.
2. Estimation of residual stress components in regions of the disc where the measured orthogonal strains were thought to lie in principal directions provided reasonable agreement with model results. However, significant internal shear stresses (up to 180 MPa) were predicted where the upper and lower surfaces of the forging were inclined appreciably to the disc axis. For this reason, caution is advised when attempting to simplify internal strain measurements in complex axisymmetric components; measurement of strain in a fourth direction to obtain the full strain tensor is recommended.
3. The general state of residual stress in the disc was one of near-surface compression, balanced by tension within the disc interior; classical stress reversal was predicted to occur due to differential contraction during the quenching process. The largest individual component was the hoop stress, reaching 400 to 500 MPa near the surface and at the core of the disc. This is well in excess of the material yield stress because of the presence of significant internal hydrostatic stress. Model predictions indicate that almost the entire disc is maintained at the effective stress necessary for yielding, except at about 10 mm below the surface, where the transition from tension to compression occurs. Hence, the overall stress state is highly sensitive to the room-temperature flow stress adopted during modeling. On the other hand, the precise location of the tension-compression transition is likely to depend on the high-temperature properties of the alloy.
4. Coupled thermal-mechanical finite-element modeling provides a virtual capability for the prediction of residual stress and distortion in engineering components and structures. Future efforts directed toward the refinement of input parameters and boundary conditions would further improve the accuracy of model predictions.

ACKNOWLEDGMENTS

This work was carried out as part of a multidisciplinary research program involving contributions from QinetiQ plc, Wyman-Gordon Ltd., Rolls-Royce plc, Special Metals Wiggin Ltd., University of Birmingham (Birmingham, United Kingdom), and Imperial College (London). The research was partly funded under the United Kingdom Engineering and Physical Sciences Research Council Grant No. GR/N14101.

REFERENCES

1. X. Xu, W. Zhang, and P.D. Lee: *Metall. Mater. Trans. A*, 2002, vol. 33A, pp. 1805-15.
2. A. Kermanpur, W. Wang, P.D. Lee, and M. McLean: *Mater. Sci. Technol*., 2003, vol. 19, pp. 859-65.
3. C.A. Dandre, S.M. Roberts, R.W. Evans, and R.C. Reed: *Mater. Sci. Technol*., 2000, vol. 16, pp. 14-25.
4. G.S. Shen, S.L. Semiatin, and R. Shivpuri: *Metall. Mater. Trans. A*, 1995, vol. 26A, pp. 1795-1803.
5. A. Kermanpur, S. Tin, P.D. Lee, and M. McLean: *JOM*, 2004, vol. 56, pp. 72-78.
6. S. Tin, P.D. Lee, A. Kermanpur, M.A. Rist, and M. McLean: *Metall. Mater. Trans A*, 2005, vol. 36A, pp. 2493-504.
7. J.A. Dann, M.R. Daymond, L. Edwards, J.A. James, and J.R. Santisteban: *Physica B*, 2004, vol. 350, pp. e511-e514.
8. F. Abbasi and A.J. Fletcher: *Mater. Sci. Technol*., 1985, vol. 1, pp. 830-37.
9. Y. Nagasaka, J.K. Brimacombe, E.B. Hawbolt, I.V. Samarasekera, B. Hernandezmorales, and S.E. Chidiac: *Metall. Trans A*, 1993, vol. 24A, pp. 795-808.
10. D.Y. Ju, R. Mukai, N. Minakawa, Y. Morii, and A. Moriai: *Key Eng. Mater*., 2004, vols. 270–273, pp. 139-46.
11. R.A. Wallis and P.R. Bhowal: *Superalloys 1988*, TMS, Warrendale, PA, 1988, pp. 525-34.
12. J.M. Franchet, F. Devy, P.E. Mosser, Y. Honnorat, and A. Benallal: *Superalloys 1992*, TMS, Warrendale, PA, 1992, pp. 73-82.
13. D. Dye, K.T. Conlon, and R.C. Reed: *Metall. Mater. Trans. A*, 2004, vol. 35A, pp. 1703-13.
14. U. Cihak, P. Staron, W. Marketz, H. Leitner, J. Tockner, and H. Clemens: *Z. Metallkd*., 2004, vol. 95, pp. 663-67.
15. M.R. Daymond, M.A.M. Bourke, R.B. Von Dreele, B. Clausen, and T. Lorentzen: *J. Appl. Phys*., 1997, vol. 82, pp. 1554-62.
16. M.R. Daymond: *J. Appl. Phys*., 2004, vol. 96, pp. 4263-72.
17. J.A. James, J.R. Santisteban, L. Edwards, and M.R. Daymond: *Physica B*, 2004, vol. 350, pp. e743-e746.
18. *DEFORM 2D, Version 8.1*, Scientific Forming Technologies Corporation, Columbus, OH, 2004.
19. J. Kolts: in *Superalloy 718—Metallurgy and Applications*, TMS, Warrendale, PA, 1989, pp. 329-44.
20. Anon: *Adv. Mater. Processes*, 2000, vol. 158, pp. 89-102.
21. D. Dye, O. Hunziker, S.M. Roberts, and R.C. Reed: *Metall. Mater. Trans. A*, 2001, vol. 32A, pp. 1713-25.
22. "High-Temperature High-Strength Nickel-Base Alloys," Technical Report No. 393, Nickel Development Institute, 1995, pp. 1-52.
23. K.C. Mills: *Recommended Values of Thermophysical Properties for Selected Commercial Alloys*, Woodhead Publishing, Cambridge, United Kingdom, 2002, pp. 181-90.
24. M. Kobayashi, A. Ono, M. Otsuki, H. Sakate, and F. Sakuma: *Int. J. Thermophys*., 1999, vol. 20, pp. 299-308.
25. *ASM Handbook Volume 4: Heat Treating*, ASM INTERNATIONAL, Materials Park, OH, 1991, pp. 803-14.
26. S. Sen, B. Aksakal, and A. Ozel: *Int. J. Mech. Sci*., 2000, vol. 42, pp. 2013-29.